

# Discovery of SXP 265, a Be/X-ray binary pulsar in the Wing of the Small Magellanic Cloud <sup>★</sup>

R. Sturm,<sup>1</sup> F. Haberl,<sup>1</sup> G. Vasilopoulos,<sup>1</sup> E. S. Bartlett,<sup>2</sup> P. Maggi,<sup>1</sup> A. Rau,<sup>1</sup>  
J. Greiner<sup>1</sup> and A. Udalski<sup>3</sup>

<sup>1</sup>Max-Planck-Institut für extraterrestrische Physik, Giessenbachstraße, 85748 Garching, Germany

<sup>2</sup>Astrophysics, Cosmology and Gravity Centre (ACGC), Astronomy Department, University of Cape Town, Private Bag X3, Rondebosch, 7701, South Africa

<sup>3</sup>Warsaw University Observatory, Aleje Ujazdowskie 4, 00-478 Warsaw, Poland

Accepted 2014 August 14. Received 2014 August 14; in original form 2014 July 22

## ABSTRACT

We identify a new candidate for a Be/X-ray binary in the *XMM-Newton* slew survey and archival *Swift* observations that is located in the transition region of the Wing of the Small Magellanic Cloud and the Magellanic Bridge. We investigated and classified this source with follow-up *XMM-Newton* and optical observations. We model the X-ray spectra and search for periodicities and variability in the X-ray observations and the OGLE *I*-band light curve. The optical counterpart has been classified spectroscopically, with data obtained at the SAAO 1.9 m telescope, and photometrically, with data obtained using GROND at the MPG 2.2 m telescope. The X-ray spectrum is typical of a high-mass X-ray binary with an accreting neutron star. We detect X-ray pulsations, which reveal a neutron-star spin period of  $P_s = (264.516 \pm 0.014)$  s. The source likely shows a persistent X-ray luminosity of a few  $10^{35}$  erg s<sup>−1</sup> and in addition type-I outbursts that indicate an orbital period of  $\sim 146$  d. A periodicity of 0.867 d, found in the optical light curve, can be explained by non-radial pulsations of the Be star. We identify the optical counterpart and classify it as a B1-2II-IVe star. This confirms SXP 265 as a new Be/X-ray binary pulsar originating in the tidal structure between the Magellanic Clouds.

**Key words:** galaxies: individual: Small Magellanic Cloud – galaxies: stellar content – stars: emission-line, Be – stars: neutron – X-rays: binaries.

## 1 INTRODUCTION

Besides supergiant high-mass X-ray binaries, Be/X-ray binaries (BeXRBs, for a review see Reig 2011) are the dominant subclass of high-mass X-ray binaries (HMXBs). They consist of a Be star orbited by a compact object, usually a neutron star (NS). Be stars primarily eject material in the equatorial plane, building up a decretion disc, which leads to observable emission lines (e.g. H $\alpha$ ) in the optical spectrum and an excess emission in the near infrared (NIR). Both are potentially variable due to instabilities in the disc and interaction with the NS. X-ray outbursts are observed when the NS accretes enhanced amount of material from this decretion disc, particularly during periastron passage (type-I,  $L_X \gtrsim 10^{36}$  erg s<sup>−1</sup>) or decretion disc instabilities (type-II,  $L_X \gtrsim 10^{37}$  erg s<sup>−1</sup>), but persistent X-ray emission is also observed in some systems ( $L_X \sim 10^{35}$  erg s<sup>−1</sup>).

Because of recent star formation, the Magellanic Clouds har-

bour a large population of BeXRBs that is well observable with today's X-ray observatories owing to the short distance of 50–60 kpc and a relatively small absorbing foreground column density of a few  $10^{20}$  cm<sup>−2</sup>. These systems enable a wealth of possible physical studies. Prominent examples are the recently discovered pulsar LXP 169 (Maggi et al. 2013), which shows optical transits likely caused by material captured by the NS, and SXP 1062 (Hénault-Brunet et al. 2012; Haberl et al. 2012; Sturm et al. 2013a), which is associated to a supernova remnant allowing a robust age determination. Both systems can be used to constrain accretion physics. In addition to individually interesting sources, the known population of the Magellanic Clouds is as comprehensive as the Galactic sample and ideally suited for statistical studies, e.g. to determine the NS spin distribution (Knigge et al. 2011; Cheng et al. 2014), the relation to the star-formation history (Antonioni et al. 2010), and the faint end of the X-ray luminosity function (Shtykovskiy & Gilfanov 2005; Sturm et al. 2013c), and to find and constrain the population of Be/white dwarf systems (Kahabka et al. 2006; Sturm et al. 2012; Li et al. 2012; Morii et al. 2013).

We have been granted two triggered *XMM-Newton* observations in AO 12 to follow up hard X-ray transients in the Magel-

<sup>★</sup> Based on observations with XMM-Newton, an ESA Science Mission with instruments and contributions directly funded by ESA Member states and the USA (NASA)

lanic Clouds and to get a more complete sample of pulsars in these galaxies. The first source observed was RX J0520.5-6932 in the Large Magellanic Cloud (LMC) leading to the discovery of the pulse period and a characterisation of the X-ray spectrum during a type-I outburst as presented by Vasilopoulos et al. (2014). Here, we present the results from the second observation, that led to the discovery of a new pulsar, SXP 265, located in the intersection of the Wing of the Small Magellanic Cloud (SMC) and the Magellanic Bridge, a tidal structure connecting the LMC and SMC with a continuous stream of gas and young stars (Skowron et al. 2014). This region has a different star-formation history (Harris & Zaritsky 2004; Harris 2007) and metallicity (Dufton et al. 2008) to the Bar of the SMC, which harbours most of the known SMC BeXRBs, and so it is particularly interesting to find more BeXRBs in this region.

This paper is structured as follows: In Section 2, we describe the observations and reduction of the data, followed by the analysis in Section 3, the discussion of the results in Section 4, and a summary in Section 5.

## 2 OBSERVATIONS AND DATA REDUCTION

### 2.1 XMM-Newton

*XMM-Newton* (Jansen et al. 2001) carries three X-ray telescopes with the European Photon Imaging Camera (EPIC, Turner et al. 2001; Strüder et al. 2001) instrument at the focal point of each. Between observations, the EPIC-pn operates with the medium filter whilst slewing, allowing for detections of sources with flux  $F > 1.2 \times 10^{-12}$  erg cm $^{-2}$  s $^{-1}$  in the (0.2–12.0) keV band. These sources are included in the *XMM-Newton* slew-survey catalogue (Saxton et al. 2008).

We found SXP 265 in an investigation of *XMM-Newton* slew-survey detections in the field of the Magellanic Clouds. The source is listed as XMMSL1 J013250.6-742544 and was initially detected on 2007 June 4, followed by a second slew detection on 2007 October 28. A third slew detection on 2011 October 17 is listed as XMMSL1 J013251.0-742549 in the 1.6 release of the slew-survey catalogue. Using a *Swift* observations on 2013 October 23 (see Section 2.2), we found the source in a bright outburst allowing us to trigger a pointed *XMM-Newton* observation performed 4 days later (MJD 56 592.7–56 593.1). The observation log is presented in Table 1.

The data of the pointed observation of all three EPIC instruments were processed with SAS 13.0.0<sup>1</sup>. Time intervals of high background have been rejected by selecting background rates in the (7.0–15.0) keV band below 8 cts ks $^{-1}$  arcmin $^{-2}$  for EPIC-pn and below 2.5 cts ks $^{-1}$  arcmin $^{-2}$  for both EPIC-MOS. Events were extracted within a circular region around the source the radii of which was determined with the SAS task `EREGIONANALYSE` to optimise the signal-to-noise ratio. For the selection of background events, we used a circular extraction region of a source-free area on the same CCDs as the source. For the creation of spectra and response matrices with `ESPECGET`, we used single- and double-pixel events of EPIC-pn and single- to quadruple-pixel events of EPIC-MOS with `FLAG=0`. All spectra were binned for a signal-to-noise ratio of at least 5 in each bin. Time series were extracted with the same pattern selection but using all events independent of flags. The photon arrival times were randomised within the CCD frame time

and recalculated for the solar-system barycentre. A merged time series for all three instruments was created, using only simultaneous good-time intervals for all instruments.

### 2.2 Swift

SXP 265 was observed independently with the *Swift* satellite. The source is listed as SWIFT J0132.5-7425, an unidentified X-ray source, in the *Swift*/BAT 58-month hard X-ray survey catalogue, but is not included in the 70-month BAT catalogue (Baumgartner et al. 2013). SWIFT J0132.5-7425 was observed with two *Swift*/XRT exposures in 2010, also listed in Table 1. The corresponding X-ray source in the 7-year Swift-XRT point-source catalogue (D’Elia et al. 2013) is 1SWXRT J013251.3-742545. We requested further *Swift* observations in 2013, after identifying the source as a BeXRB candidate.

*Swift*/XRT spectra were extracted from the cleaned level-3 event files with the `FTOOL2 XSELECT` using circular extraction regions for the source and background. The spectra were not binned due to the low statistics. Ancillary response files were created using `XRTMKARF`.

### 2.3 GROND

On 2013 October 28 03:29 UT, close to the time of the *XMM-Newton* observation, we observed SXP 265 with the Gamma-ray Burst Optical Near-ir Detector (GROND, Greiner et al. 2008) at the MPG 2.2 m telescope in La Silla, Chile. 141 s of integration were obtained in  $g'$ ,  $r'$ ,  $i'$ , and  $z'$  and 240 s in  $J$ ,  $H$ , and  $K_s$ . The data were reduced and analysed with the standard tools and methods described in Krühler et al. (2008). The  $g'$ ,  $r'$ ,  $i'$ , and  $z'$  photometric calibration was obtained relative to an observation of an SDSS standard star field obtained  $\sim 1$  h earlier. The  $J$ ,  $H$ , and  $K_s$  photometry was calibrated against selected 2MASS stars (Skrutskie et al. 2006). The derived AB magnitudes including systematic uncertainties, but not corrected for foreground reddening, are:  $g' = 14.87 \pm 0.02$ ,  $r' = 15.20 \pm 0.03$ ,  $i' = 15.44 \pm 0.04$ ,  $z' = 15.59 \pm 0.07$ ,  $J = 15.92 \pm 0.07$ ,  $H = 16.12 \pm 0.08$ , and  $K_s = 16.70 \pm 0.11$  mag.

### 2.4 OGLE

SXP 265 has been monitored regularly in the  $I$  and  $V$  band during the phase IV of the Optical Gravitational Lensing Experiment (OGLE, Udalski et al. 2008) since 2010 August 6 (MJD 55 414). The OGLE source identification is SMC739.11.1265. In this study, we use data until 2014 January 12 (MJD 56 669), containing 341  $I$ -band and 29  $V$ -band measurements collected in four seasons. Ongoing observations are accessible with the X-Ray variables OGLE Monitoring (XROM, Udalski 2008) system.

### 2.5 SAAO 1.9 m

The optical spectra were taken with the 1.9 m Radcliffe telescope at the South African Astronomical Observatory (SAAO) on the night of 2013 November 5 (MJD 56 601) with an exposure time of 1500 s. A 600 lines mm $^{-1}$  reflection grating was used, blazed at

<sup>1</sup> Science Analysis Software (SAS), <http://xmm.esa.int/sas/>

<sup>2</sup> <http://heasarc.nasa.gov/ftools/>

**Table 1.** X-ray observations of SXP 265.

Observation	ObsID	Start time (UT)	End time (UT)	Instrument	Mode <sup>a</sup>	Net Exp [ks]	Net Cts <sup>b</sup>	R <sub>sc</sub> <sup>c</sup> [']
XMM 2013	0724650301	2013 Oct 27 16:24	2013 Oct 28 01:46	EPIC-MOS1	ff–medium	24.0	3678	48
		16:24	01:46	EPIC-MOS2	ff–medium	24.0	4502	54
		16:47	01:42	EPIC-pn	ff–thin	20.2	11 904	46
Swift 2010 a	00040893001	2010 Sep 22 01:10	2010 Sep 22 23:50	XRT	pc	6.6	52	40
Swift 2010 b	00040893002	2010 Oct 01 11:22	2010 Oct 01 16:33	XRT	pc	2.1	18	40
Swift 2013 a	00040893003	2013 Feb 16 16:46	2013 Feb 16 18:41	XRT	pc	2.0	41	40
Swift 2013 b	00040893004	2013 Oct 23 13:59	2013 Oct 23 15:56	XRT	pc	2.1	160	40
Swift 2013 c	00040893006	2013 Oct 31 10:58	2013 Oct 31 12:45	XRT	pc	2.1	65	40

<sup>a</sup> Observation setup and filter: full-frame mode (ff) and photon-counting mode (pc).

<sup>b</sup> Net counts as used for spectral analysis in the (0.2–12.0) keV band for *XMM-Newton* and in the (0.3–7.0) keV band for *Swift*.

<sup>c</sup> Radius of the circular source extraction region.

**Table 2.** Spectral-fit results for SXP 265.

Observation	Model <sup>a</sup>	N <sub>H,SMC</sub> <sup>b</sup>	Γ	kT <sup>c</sup>	R <sup>d</sup>	F <sup>e</sup>	L <sub>x</sub> <sup>f</sup>	χ <sub>v</sub> <sup>2</sup>	ν
XMM 2013	PL	1.07 <sup>+0.21</sup> <sub>-0.20</sub>	0.820 <sup>+0.022</sup> <sub>-0.021</sub>	–	–	3.836 ± 0.077	1.83 <sup>+0.03</sup> <sub>-0.03</sub>	1.16	583
	DiskBB	0.711 <sup>+0.15</sup> <sub>-0.14</sub>	–	6100 <sup>+540</sup> <sub>-450</sub>	0.101 <sup>+0.012</sup> <sub>-0.012</sub>	3.716 ± 0.080	1.77 <sup>+0.03</sup> <sub>-0.03</sub>	1.03	583
	PL+BB	4.58 <sup>+0.98</sup> <sub>-0.88</sub>	0.914 <sup>+0.034</sup> <sub>-0.029</sub>	63.7 <sup>+5.4</sup> <sub>-5.8</sub>	880 <sup>+610</sup> <sub>-340</sub>	3.786 ± 0.076	2.88 <sup>+0.32</sup> <sub>-0.45</sub>	1.07	581
	PL+BB 2	0.493 <sup>+0.23</sup> <sub>-0.17</sub>	0.825 <sup>+0.055</sup> <sub>-0.052</sub>	1280 <sup>+142</sup> <sub>-142</sub>	1.20 <sup>+0.19</sup> <sub>-0.16</sub>	3.790 ± 0.050	1.70 <sup>+0.02</sup> <sub>-0.02</sub>	0.99	581
	PL+DiskBB	4.60 <sup>+0.95</sup> <sub>-0.93</sub>	0.926 <sup>+0.032</sup> <sub>-0.030</sub>	73.4 <sup>+7.0</sup> <sub>-7.4</sub>	800 <sup>+600</sup> <sub>-320</sub>	3.785 ± 0.078	3.37 <sup>+1.43</sup> <sub>-0.69</sub>	1.07	581
Swift 2010 a	PL	<1.6	0.82 ± 0.34	–	–	0.69 ± 0.17	0.33 <sup>+0.08</sup> <sub>-0.07</sub>	–	–
Swift 2010 b						0.89 ± 0.41	0.43 <sup>+0.19</sup> <sub>-0.14</sub>		
Swift 2013 a	PL	<3.4	0.75 <sup>+0.15</sup> <sub>-0.20</sub>	–	–	2.02 ± 0.56	0.96 <sup>+0.25</sup> <sub>-0.21</sub>	–	–
Swift 2013 b						7.06 ± 0.96	3.37 <sup>+0.43</sup> <sub>-0.39</sub>		
Swift 2013 c						2.87 ± 0.63	1.37 <sup>+0.28</sup> <sub>-0.25</sub>		

<sup>a</sup> For definition of spectral models see Section 3.1.

<sup>b</sup> Column density within the interstellar medium of the SMC or intrinsic to the source in 10<sup>21</sup> cm<sup>-2</sup>.

<sup>c</sup> Temperature in keV.

<sup>d</sup> Radius of the emitting area (for BB) or inner-disc radius for an inclination of Θ = 0 (for DiskBB) in km.

<sup>e</sup> Observed flux in the (0.2–10.0) keV band in 10<sup>-12</sup> erg cm<sup>-2</sup> s<sup>-1</sup>. For the *Swift* spectra, the best-fit power-law model derived from the *XMM-Newton* data has been used to estimate the fluxes.

<sup>f</sup> Source intrinsic X-ray luminosity in the (0.2–10.0) keV band in 10<sup>36</sup> erg s<sup>-1</sup>, corrected for absorption and assuming a distance of the source of 62.1 kpc.

4600 Å, along with the SiTe CCD. A slit width of 1.5'' was employed. This resulted in a wavelength range of λλ3500 – 5500 Å and a resolution of ~ 3.0 Å, determined from the full width half maximum of the arc lines in the comparison spectra. This corresponds to 2.7 pixels on the CCD. The median signal-to-noise ratio in the λλ4000 – 5000 Å region is ~33, ranging from ~17 to 74.

The data were reduced using the standard packages available in the Image Reduction and Analysis Facility (IRAF). Wavelength calibration was implemented using comparison spectra of copper and argon lamps taken immediately before and after the observation with the same instrument configuration. The spectrum was normalised and a redshift correction applied corresponding to a recession velocity of the SMC of 158 km s<sup>-1</sup> (Richter, Tammann & Huchtmeier 1987).

### 3 ANALYSES AND RESULTS

#### 3.1 X-ray spectrum

The three EPIC spectra were fit simultaneously using *XSPEC* (Arnaud 1996) version 12.7.0. A constant factor was included and allowed to vary for instrumental differences. We find  $C_{\text{MOS1}} = 1.07 \pm 0.04$  and  $C_{\text{MOS2}} = 1.04 \pm 0.03$  relative to EPIC-pn ( $C_{\text{pn}} = 1$ ), consistent with the current cross-calibration discrepancy. All other parameters for various models were forced to be the same for all instruments and are listed in Table 2 with 90 per cent confidence uncertainties ( $\Delta\chi^2 = 2.71$ ). The photoelectric absorption within the Galaxy was calculated assuming a column density of  $N_{\text{H,Gal}} = 4 \times 10^{20}$  cm<sup>-2</sup> (Dickey & Lockman 1990) with solar abundances (according to Wilms et al. 2000). Additional absorption

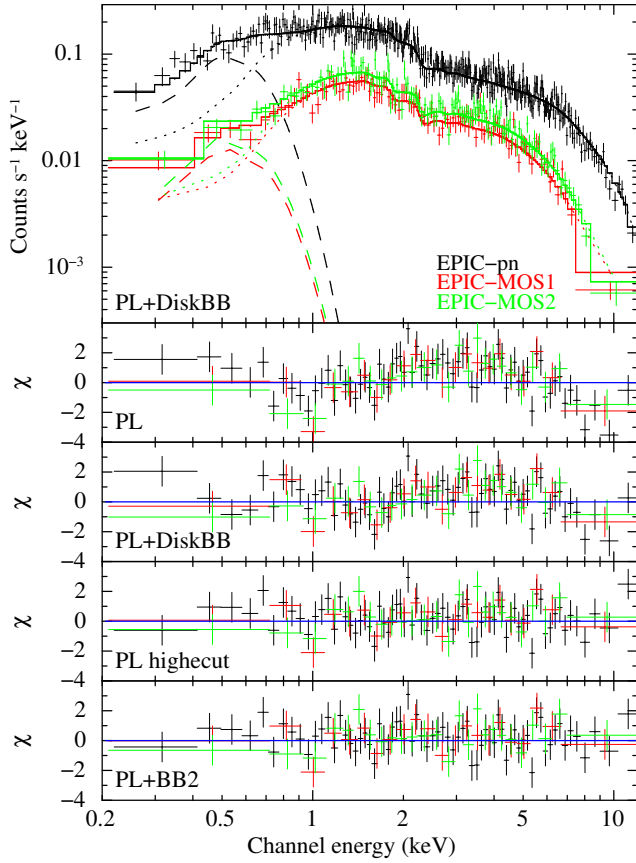


**Figure 1.** The X-ray spectra of SXP 265 as observed with *XMM-Newton* together with the folded best-fit model (solid lines) of a power law (dotted lines) and a multi-temperature disc (dashed lines) are plotted in the *upper panel*. EPIC-pn/MOS1/MOS2 data are plotted in black/red/green. The residuals for a simple power-law, a power-law and disc, power-law with high-energy cut, and power-law and hot black-body model are plotted in the *lower panels* (from top to bottom). For clarity, the residuals have been rebinned by a factor of 5.

by material within the interstellar medium of the SMC or intrinsic to the source was determined by the fit with abundances set to  $Z = 0.2Z_{\odot}$  (Russell & Dopita 1992). The spectra are described satisfactorily by an absorbed power law with  $\chi^2_{\nu} = 1.15$  (with  $\nu = 583$  degrees of freedom), but this fit exhibits systematic residuals in all instruments (second panel from top in Fig. 1).

We found a disc black-body model to be a better fit to the data, but this requires physically implausible parameters. Alternatively, we can account for a steeper spectral shape at higher energies with a broken power-law model, which results in  $\chi^2_{\nu} = 1.00$ ,  $\Gamma_1 = 0.60$ ,  $\Gamma_2 = 1.1$ , and a break energy of  $E_{br} = 3.19$  keV, or with a power-law model containing an additional high-energy cut off, which results in  $\chi^2_{\nu} = 1.00$ ,  $\Gamma = 0.56 \pm 0.08$ , a cut-off energy of  $E_{cut} = 2.32 \pm 0.03$  keV, and a folding energy of  $E_{fold} = 10.5^{+2.4}_{-1.6}$  keV. We note, that a simultaneous fit to the *Swift*/BAT spectrum with this cut-off model (with free model normalisation,  $C_{BAT} = 1.4 \pm 0.4$ ) does not show systematic offsets in the BAT data residuals. However, since this spectrum has only 8 data bins, the fit statistics is dominated by the *XMM-Newton* spectra.

A soft emission component (e.g. Hickox et al. 2004; Eger & Haberl 2008) might be expected to contribute to the X-ray emission of HMXBs: We tested a possible contribution by adding a black-body or a multi-temperature disc black-body model. These models

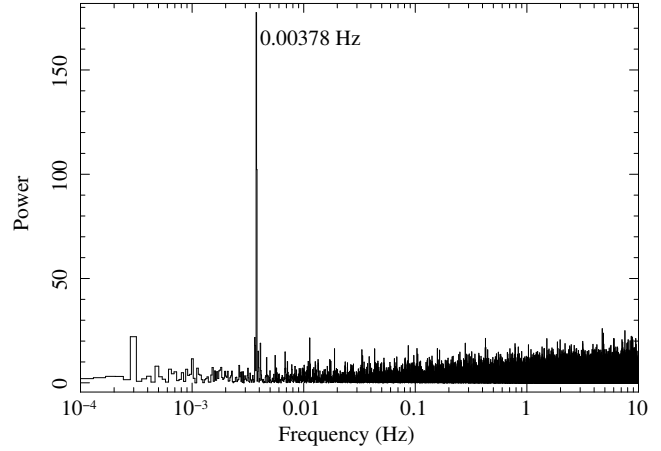


**Figure 2.** Power-density spectrum of the merged EPIC time series in the (0.2–10.0) keV band.

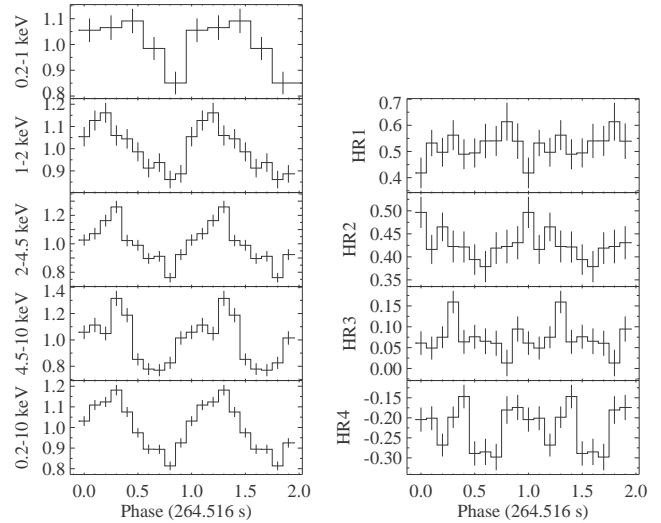


**Figure 3.** *Left:* X-ray pulse profile of SXP 265 in various energy bands of the merged time series. The pulse profiles are background-subtracted and normalised to the average net count rate of 0.14, 0.26, 0.30, 0.19 and 0.89 cts s<sup>-1</sup> from top to bottom. *Right:* Hardness ratios as a function of pulse phase derived from the pulse profiles in two neighbouring standard energy bands.

give significantly better fits with f-test probabilities of  $2 \times 10^{-8}$  and  $1 \times 10^{-8}$ . We found a second, even better, solution for a higher black-body temperature, as listed by the PL+BB 2 model in Table 2.

Another possible spectral feature of BeXRBs is Fe  $K\alpha$  line emission. By adding a Gaussian line profile with fixed central energy  $E_c = 6.4$  keV and width of  $\sigma = 0$ , we obtain a  $3\sigma$  upper limit for the line flux of  $F_{FeK\alpha} \leq 2 \times 10^{-6}$  photons cm<sup>-2</sup> s<sup>-1</sup>, which corresponds to an equivalent width of  $EW \geq -54$  eV.

The low statistics of the *Swift* spectra mean the data can be described sufficiently with the best-fit power-law model derived from the *XMM-Newton* data. When fit to the *Swift* spectra independently, the absorption and photon index are consistent with the *XMM-Newton* values within uncertainties (see Table 2). We therefore used the parameter values from the best-fit power-law model and fitted only the normalisation to the unbinned spectra with C statistics, to derive the fluxes and luminosities listed in Table 2.

### 3.2 X-ray pulsations

Using a fast Fourier transformation (FFT), we find a clear signal at a frequency of  $f = 0.00378$  Hz in the merged EPIC time series in the (0.2–10.0) keV band (Fig. 2). This period is independently seen in all three EPIC instruments. The pulse period and its  $1\sigma$  uncertainty are determined as  $P_s = (264.516 \pm 0.014)$  s using a Bayesian detection method (see Haberl et al. 2008). The folded background-subtracted EPIC light curves are presented for the total (0.2–10.0) keV band and the standard sub-bands (0.2–0.5), (0.5–1.0), (1.0–2.0), (2.0–4.5), and (4.5–10.0) keV in Fig. 3. The first two bands have been merged to increase the statistics. Variations in the hardness ratio, defined by  $HR_i = (R_{i+1} - R_i)/(R_{i+1} + R_i)$  with  $R_i$  denoting the background-subtracted count rate in the standard energy band  $i$  (with  $i$  from 1 to 4), are also shown. We estimate the pulsed fraction in the total energy band to be  $R_{\text{pulsed}}/R_{\text{total}} = 0.21 \pm 0.03$ , assuming a sinusoidal pulse profile.

### 3.3 Long-term X-ray light curve

SXP 265 is listed three times in the *XMM-Newton* slew survey catalogue (Saxton et al. 2008) as XMMSL1 J013250.6-742544 and XMMSL1 J013251.0-742549 with count rates  $(1.52 \pm 0.57) \text{ s}^{-1}$  on 2007 June 4 (MJD 54 255),  $(0.70 \pm 0.25) \text{ s}^{-1}$  on 2007 October 28 (MJD 54 401), and  $(0.85 \pm 0.41) \text{ s}^{-1}$  on 2011 October 17 (MJD 55 851), respectively.

Assuming the best-fit power-law model from above, this corresponds to (0.2–10.0) keV fluxes of  $(13.7 \pm 5.1) \times 10^{-12}$ ,  $(6.3 \pm 2.3) \times 10^{-12}$ , and  $(7.7 \pm 3.7) \times 10^{-12} \text{ erg cm}^{-2} \text{ s}^{-1}$  for an EPIC-pn exposure with medium filter.

All X-ray fluxes from pointed observations are listed in Table 2. These flux measurements reveal a variability by a factor of 10. If the *XMM-Newton* slew detections are included, variability of at least a factor of 20 becomes evident.

The long-term X-ray light curve of SXP 265 is presented in Fig. 4. Included are the upper limits from *XMM-Newton* slews without a detection of SXP 265 that were obtained from the *XMM-Newton* upper-limit server<sup>3</sup>.

Assuming a conservative detection limit of 7 cts in the ROSAT all sky survey, we obtain an upper limit of  $0.012 \text{ cts s}^{-1}$  (0.1–2.0 keV) for 1990 October. For the best-fit power-law model, this translates to a (0.2–10.0) keV flux of  $1.4 \times 10^{-12} \text{ erg cm}^{-2} \text{ s}^{-1}$  and thus does not exclude X-ray emission at the low-state level, as seen with *Swift* in 2010.

By assuming a distance of the SMC of 62.1 kpc (Graczyk et al. 2014) throughout the paper, these fluxes translate to X-ray luminosities exceeding  $10^{36} \text{ erg s}^{-1}$  for the three *XMM-Newton* slew detections and the outburst observed in 2013 October. This would be atypical for a persistent X-ray emitting state and points to X-ray outbursts. The first two slew detections are separated by 146 d and therefore unlikely to be caused by the same type-I outburst, as these last typically up to  $\sim 30$  per cent of the orbit (Galache et al. 2008). Interestingly, the third slew detection and the maximum of the 2013 outburst (*Swift* observation 2013 b), were 1451 d and 2187 d later, i.e.  $\sim 10$  times and  $\sim 15$  times the above separation. This might indicate the orbital period of the system, but needs further confirmation. We note that the X-ray light curve folded with the 146 d period includes all detections with  $L_X > 10^{36} \text{ erg s}^{-1}$  within  $\sim 10$  per

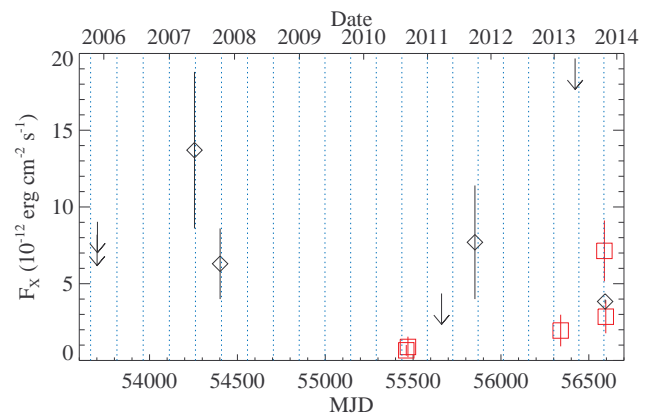


**Figure 4.** Long-term X-ray light curve including *XMM-Newton* (black diamonds) and *Swift* (red squares) detections. Upper limits from the *XMM-Newton* slew survey are marked by arrows. Dashed vertical lines indicate a 146 d period.

cent of the tentative orbital period as expected for type-I outbursts (Galache et al. 2008).

### 3.4 X-ray coordinates

The pointed *XMM-Newton* observation provides the most precise X-ray position of SXP 265. Source detection was performed on the X-ray images of all three EPIC instruments simultaneously (for details see Sturm et al. 2013c). We identified seven other X-ray sources in the field of view, to derive an astrometric correction of  $\Delta\text{RA} = -0.53''$  and  $\Delta\text{Dec} = -0.46''$ . This yields X-ray coordinates of SXP 265 of  $\text{RA} = 01^{\text{h}}32^{\text{m}}51^{\text{s}}.39$  and  $\text{Dec} = -74^{\circ}25'45''.4$  (J2000). Using astrometric corrections, the expected systematic uncertainty reduces from  $\sigma_{\text{sys}} = 1''$  to  $\sigma_{\text{sys}} = 0.35''$  (Watson et al. 2009) resulting in a  $1\sigma$  position uncertainty for SXP 265 of  $\sigma = 0.36''$ , where the statistical error is added quadratically.

This position is in agreement with the *XMM-Newton* slew detections, with angular separations of  $15.3''$  (due to the high position uncertainty this is equivalent to  $1.7\sigma$ ),  $3.9''$  ( $0.66\sigma$ ), and  $4.0''$  ( $0.76\sigma$ ), respectively. All *Swift*/XRT detections have angular separations  $< 3.3''$  ( $< 1.1\sigma$ ) and are therefore also in agreement with the *XMM-Newton* coordinates.

The *XMM-Newton* position allows us to identify 2MASS J01325144-7425453 as the optical counterpart with an angular separation of  $0.26''$ . The X-ray position is indicated in the GROND  $r'$ -band finding chart (Fig. 5). The small circle indicates the improved and the large circle the uncorrected *XMM-Newton* position. The star is also listed in the *Spitzer* SMC survey (Gordon et al. 2011) as SSTISAGEMA J013251.49-742545.2. No other object is found to be in positional agreement with the X-ray source.

### 3.5 Optical spectrum

Spectrally classifying early-type stars in the SMC is difficult due to the low metallicity environment: The metal lines required for classification using the traditional Morgan-Keenan (MK, Morgan et al. 1943) system are either much weaker or are not present. As such, the optical counterpart of SXP 265 was classified using the system developed by Lennon (1997) for B-type supergiants in the SMC, and implemented for the SMC and LMC by Evans et al.

<sup>3</sup> [http://xmm.esac.esa.int/external/xmm\\_products/slew\\_survey/upper\\_limit/uls.shtml](http://xmm.esac.esa.int/external/xmm_products/slew_survey/upper_limit/uls.shtml)

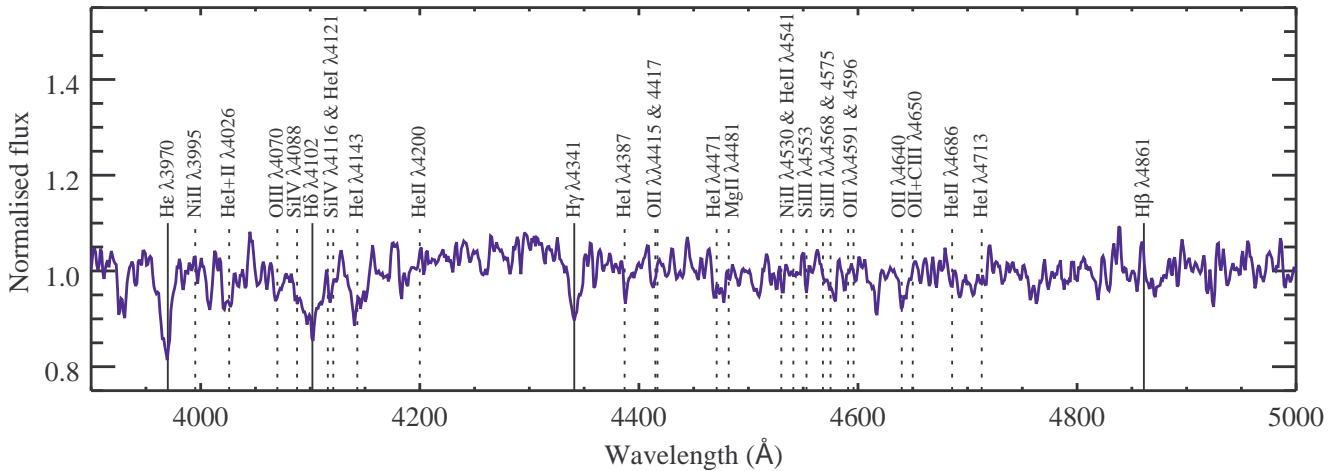


**Figure 6.** Spectrum of SXP 265 in the wavelength range  $\lambda\lambda 3900\text{--}5000$  Å taken with the Radcliffe 1.9 m telescope at SAAO on 2013 November 5. The spectrum has been normalised and redshift corrected by  $158 \text{ km s}^{-1}$ . Atomic transitions relevant to spectral classification have been marked.

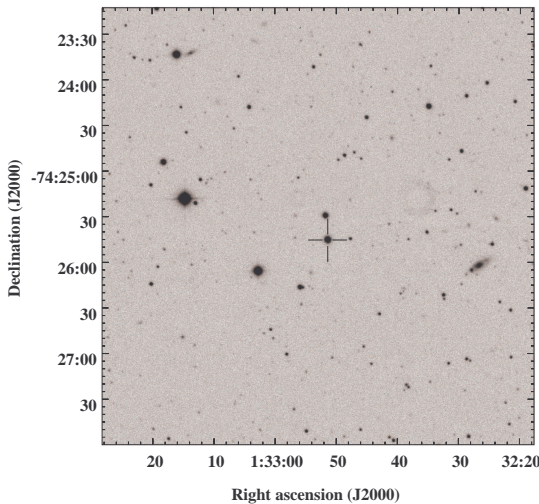


**Figure 5.** GROND  $r'$ -band finding chart. The cross marks the optical counterpart of SXP 265. In the  $8'' \times 8''$  zoom-in, the corrected and uncorrected  $1\sigma$  *XMM-Newton* positions are indicated by a small and large circle, respectively.

(2004, 2007). This system has been normalised to the MK system such that the classification criteria follow the same trends in line strengths. Figure 6 shows the normalised spectrum of SXP 265 smoothed with a boxcar average<sup>4</sup> with width 3.

Be stars are characterised by their rapid rotation. This behaviour replenishes the decretion disc where the emission lines originate, which, in turn, leads to the ‘e’ designation. It is therefore unsurprising that the optical spectrum of SXP 265 is dominated by the rotationally broadened hydrogen Balmer series. The  $H\beta$   $\lambda 4861$  line in particular shows evidence of ‘infilling’ – i.e. an emission feature superimposed on an absorption line.

The spectrum does not show any evidence for the He II  $\lambda\lambda 4200, 4541$ , or  $4686$  lines above the noise level of the data, suggesting a spectral type B1 or later. There does, however, appear

to be some evidence for the Si IV  $\lambda\lambda 4088$  and  $4116$  lines, which, if real, would constrain the spectral type to B1. The proximity of these lines to the broadened H $\gamma$  line makes it hard to determine whether they are genuine. The Si III  $\lambda 4553$  line is stronger than the Mg II  $\lambda 4481$  line constraining the spectral type to B2 or earlier.

The luminosity class of the counterpart was determined using the ratios of He I  $\lambda 4121$ /He I  $\lambda 4143$  and Si IV  $\lambda 4553$ /He I  $\lambda 4387$  (Walborn & Fitzpatrick 1990). The former decreases with increasing luminosity class (i.e. decreasing luminosity) the latter increases with increasing luminosity class. The signal-to-noise and resolution of the spectrum, along with its proximity to the Doppler broadened H $\delta$  line, make it difficult to draw any conclusions based on the He I  $\lambda 4121$  line but the Si IV  $\lambda 4553$ /He I  $\lambda 4387$  ratio suggests a luminosity class II–IV. This is supported by the strength of the O II spectrum, which also increases with increasing luminosity, however the low metallicity environment make this an unreliable luminosity-class indicator.

The well known distance to the SMC means we can calculate the absolute magnitude of the optical counterpart of SXP 265 accurately and precisely. This value can then be compared to those predicted for a B1–2II–IVe star to confirm the luminosity classification. Using the GROND  $r'$  and  $i'$  magnitudes, as well as equation 5 of Krühler et al. (2011), we get an uncorrected  $V = (15.06 \pm 0.04)$  mag. For comparison, the OGLE  $V$ -band measurements cover the range from  $V = 14.986$  to  $15.084$  mag and the one on 2013 November 4 (closest to the GROND observation) yielded  $V = (15.040 \pm 0.003)$  mag. Assuming the column density from the best-fit model to the X-ray spectrum of  $N_{\text{H,SMC}} = (5 \pm 2) \times 10^{20} \text{ cm}^{-2}$ , along with the  $N_{\text{H,Gal}}$  from Dickey & Lockman (1990,  $4 \times 10^{20} \text{ cm}^{-2}$ ) and equation 1 from Güver & Özel (2009), we derive an optical extinction of  $A_V = (0.407 \pm 0.092)$  mag. Along with a distance modulus of  $\mu = (18.95 \pm 0.07)$  mag (Graczyk et al. 2014), this implies  $M_V = (-4.3 \pm 0.1)$  mag. This value is consistent with a B1IIe star (Wegner 2006), however we note that it falls within the range of a B1–1.5Ibe star all the way down to a B1–1.5IV–Ve star. As such, we classify the optical counterpart of SXP 265 as a B1–2II–IVe star.

### 3.6 Spectral energy distribution

The simultaneously measured GROND data and the *uvw*1 measurement from the optical monitor of *XMM-Newton* were used to con-

<sup>4</sup> [http://northstar-www.dartmouth.edu/doc/idl/html\\_6.2/SMOOTH.html](http://northstar-www.dartmouth.edu/doc/idl/html_6.2/SMOOTH.html)



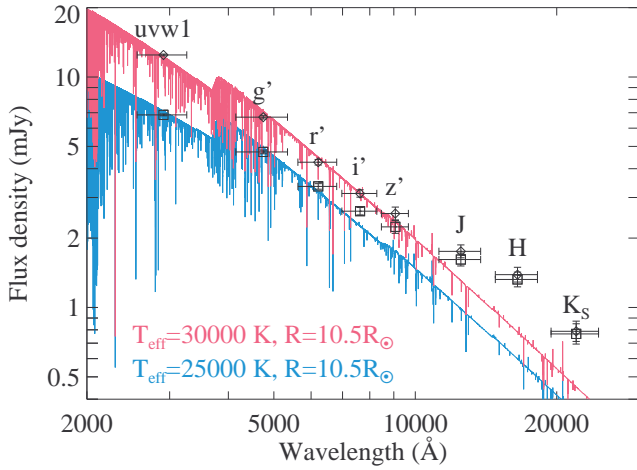


**Figure 7.** Spectral energy distribution of the optical counterpart of SXP 265 corrected for Galactic foreground reddening (squares) and for additional maximum reddening within the SMC (diamonds). The red and blue lines represent stellar atmosphere models at  $T_{\text{eff}} = 25\,000$  K and  $30\,000$  K, respectively, both for a stellar radius of  $R = 10.5R_{\odot}$ .

struct the spectral energy distribution of the source. The boxes in Fig. 7 give flux densities, corrected for the Galactic foreground reddening of  $E(B - V) = 0.044$  mag (Schlafly & Finkbeiner 2011), which we assume as the lower limit for the reddening. We assume an upper limit of the reddening within the SMC of  $E(B - V) = 0.11$  mag, which corresponds to the total line-of-sight H I column density of  $N_{\text{H,SMC}} = 6 \times 10^{20} \text{ cm}^{-2}$  (Stanimirovic et al. 1999) when using the relation of Predehl & Schmitt (1995).

We compare both spectral energy distributions with the stellar atmosphere models of Lanz & Hubeny (2007) with  $Z = 0.2Z_{\odot}$  and  $\log(g) = 4$ . The model with effective temperature  $T_{\text{eff}} = 25\,000$  K and radius  $R = 10.5R_{\odot}$  (blue line) well describes the data at shorter wavelengths in the low-extinction case. This temperature is typical for a B1 star. The radius is somewhat larger than that expected for a main-sequence star. In the high-extinction case, a  $T_{\text{eff}} = 30\,000$  K (red line) is needed to compensate for the high extinction in the UV, this temperature is more typical of a B0 star.

The uncertainty in the proper extinction correction has the greatest effect towards the UV. However, towards the NIR, the re-processing of the UV radiation from the star by the decretion disc is expected to cause an additional emission component. For both extinction scenarios, we find a clear indication for such an excess in the  $H$  and  $K_S$  band.

### 3.7 Optical light curve

The OGLE-IV  $I$ -band light curve, presented in the middle panel of Fig. 8, reveals long-term variability, e.g. by a systematic increase of  $\sim 0.2$  mag in the  $I$  band between 2010 August and 2011 July (MJD 55 414–55 745). Another, even stronger, brightening of the source is found between 2MASS (1998 October 8, MJD 51 094) and 2MASS6X (2000 December 8, MJD 51 886) observations (Skrutskie et al. 2006) by  $(0.922 \pm 0.072)$  mag in the  $J$  band,  $(1.07 \pm 0.19)$  mag in the  $H$  band, and  $> 0.5$  mag in the  $K$  band.

We obtained  $V - I$  colours using the OGLE  $V$ -band observations closest in time to the  $I$ -band observations, with a maximal separation of one day. This resulted in 9 and 18 colour measurements in the first and second OGLE season, respectively, as plotted

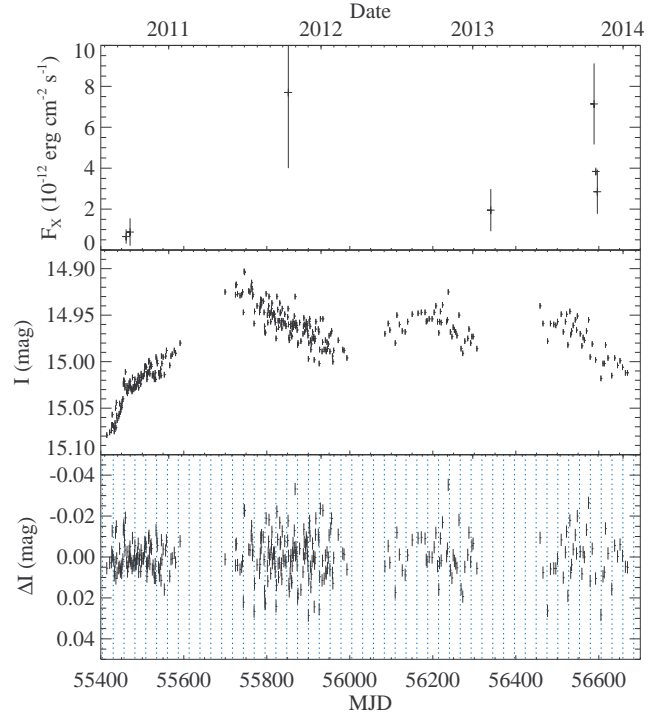


**Figure 8.** Upper panel: X-ray light curve in the (0.2–10.0) keV band. Middle panel: OGLE  $I$ -band light curve. Lower panel: Detrended OGLE  $I$ -band light curve. Dashed vertical lines mark a 26.13 d period.

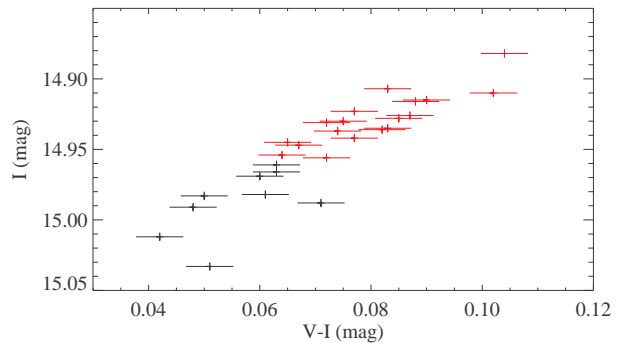


**Figure 9.** OGLE colour-magnitude diagram for SXP 265 from the first (black) and second (red) season.

in Fig. 9. A clear correlation is seen between the parameters: The source becomes redder with increasing brightness. This is expected if the inclination of the decretion disc is  $\lesssim 80^\circ$  with respect to the observer (Rajaelimanana, Charles & Udalski 2011).

The Lomb-Scargle periodogram (Scargle 1982) of the detrended OGLE light curve, between 2011 May and 2014 January (season 2–4, MJD 55 699–56 669), is presented in Fig. 10. The significant peaks are found at 6.532, 1.177, 0.867, 0.541, 0.464, 0.351, and 0.317 d as labelled in Fig. 10. These are 1-day aliases of each other caused by the sampling. Whereas the strongest power is found for the 6.532 d period when using the seasons 2–4, the 0.867 d period has a similar power to the 6.532 d period, if only season 2 is used (22.00 vs. 22.02). No significant detections are seen when the other seasons are independently investigated. The folded light curves for both periods are sinusoidal (Fig. 11) and have small

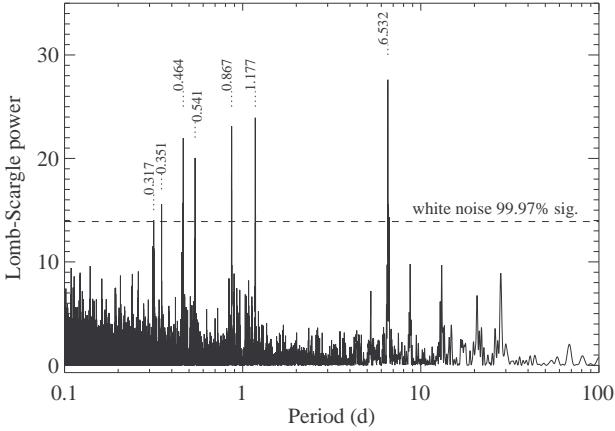


**Figure 10.** Lomb-Scargle periodogram of the detrended OGLE light curve excluding the measurements before MJD 55 600. The maxima of the strongest peaks are labelled.

amplitudes of  $(0.00699 \pm 0.00028)$  and  $(0.00754 \pm 0.00028)$  mag, respectively.

To estimate the uncertainties in both periods, we use the bootstrap method (Efron 1982). We created random light curves from the original OGLE measurements by sampling with replacement (i.e. one epoch can be drawn multiple times) and searched for periodicities. We repeated the above procedure 1000 times allowing the  $1\sigma$  uncertainties to be determined from the resulting distribution as  $(6.532 \pm 0.012)$  and  $(0.867 \pm 0.010)$  d.

In Fig. 11, we also show the light curve convolved at 26.13 d, i.e. 4 times the 6.532 d period. In this case, we see a stronger dip and increase at phase  $\sim 0.5$  than at the other expected minima. These phases are also marked in the detrended light curve with vertical lines in Fig. 8. We note that these dips are not present in the first season, when the source was brightening but still in a fainter state.

The total OGLE light curve covers 1254 days allowing periods up to  $\sim 600$  d to be resolved. The Lomb-Scargle periodogram of the unaltered light curve (i.e. without detrending) shows strong power at  $\sim 241$  and  $\sim 643$  d (in addition to the 1 and 6.53 d periods) and the  $\sim 346$  d that is seen when the first season is not used. Due to the limited statistics and additional long-term variability, a longer coverage of the source is needed to establish the orbital period of the NS from optical variability.

## 4 DISCUSSION

The X-ray spectrum, X-ray pulsations, and the identification of the optical counterpart as a Be star allow us to clearly identify SXP 265 as a neutron-star BeXRB. Its properties are discussed in the following.

### 4.1 Spectra

The precise *XMM-Newton* coordinates allow us to clearly identify 2MASS J01325144-7425453 as the optical counterpart. Our spectral classification of a B1-2II-IVe star is typical for a BeXRB in the SMC, as these are primarily found between O9.5 and B1.5 (McBride et al. 2008). Irregular long-term optical variability and excess emission in the NIR are observed. This is typical for Be stars

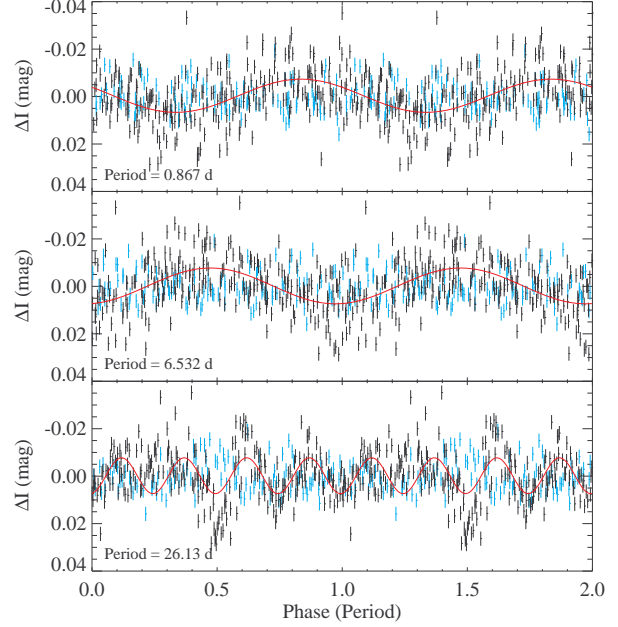


**Figure 11.** Folded detrended OGLE light curve for several periods. The first season is plotted in cyan, others in black. The red line gives the best-fit sine function. In the lower panel, the sine function has a period of 6.532 d.

and likely caused by a varying amount of reprocessing material in the decretion disc around the Be star.

The overall X-ray spectrum follows a power-law model with a typical photon index for BeXRBs in the SMC (Haberl & Pietsch 2004). Evidence for a moderate deviation from this model is seen in the residuals. This could be due to the contribution of a low temperature ( $kT \sim 100$  eV) soft excess. The inferred values are typical of those found in other BeXRBs (e.g. Haberl & Pietsch 2008; Sturm et al. 2011) and allow for a soft excess with bolometric luminosity up to  $L_{\text{bol}} = 1.6^{+1.9}_{-0.8} \times 10^{36}$  erg s $^{-1}$ . However, these models require a high absorbing column. The derived radius of the emission region, estimated according to Hickox et al. (2004), is  $R = (L_X/4\pi\sigma T^4)^{1/2} = 756$  km; too large for an NS. We attribute this excess to an accretion disc or X-ray reprocessing material around the NS.

A contribution by a thermal component with higher temperature ( $kT > 1$  keV) is also possible (La Palombara et al. 2013; Bartlett et al. 2013). For some sources this solution results in a physically questionable scenario, with the power-law component dominating the spectrum at lower energies and the black-body component contributing most of emission at higher energies. In this case, however, the black-body component contributes 20 per cent to the measured (0.2–10.0) keV flux and the flux density of the black-body is below that of the power-law component at all energies. A possible interpretation for the origin of this component is emission from the heated polar caps of the NS. The radius is at the upper limit of what is usually reported, but a slowly spinning NS with a rather constant X-ray luminosity is in agreement with this picture. An indication of spectral variability at higher energies is seen in the *HR* variations (Fig. 3), but the statistics is insufficient for a detailed phase-resolved spectral analysis.

We also derived good fits using a power-law model with a high-energy cut off. In other HMXBs such a cut off is observed



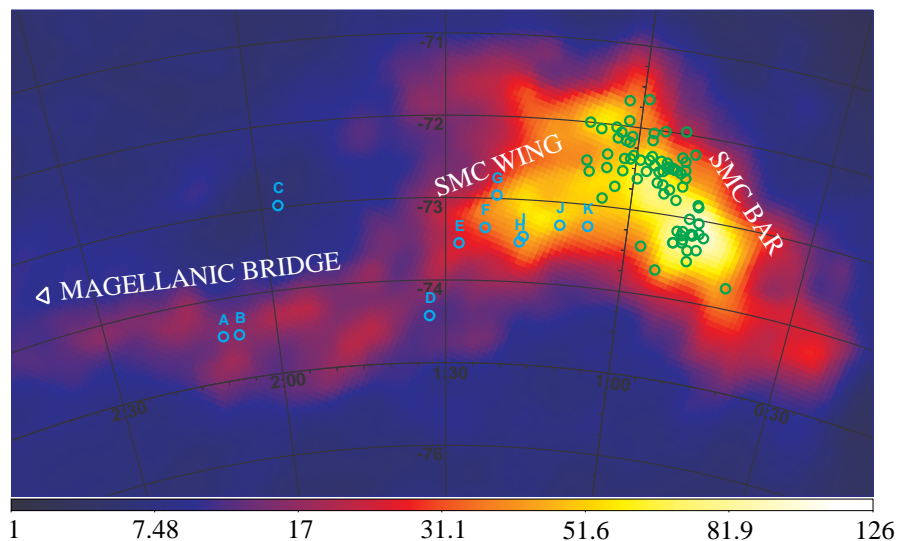


**Figure 12.** Spatial distribution of HMXB in the SMC compared to the H I column density in  $10^{20} \text{ cm}^{-2}$  from McClure-Griffiths et al. (2009). BeXRBs and candidates in the SMC Bar are marked with green circles. HMXBs in the Wing and Bridge are plotted with cyan circles and labelled as follows: <sup>(A)</sup> RXJ 0209.6-7427 (Kahabka & Hilker 2005), <sup>(B)</sup> SWIFT J0208.4-7428 (McBride et al. 2010), <sup>(C)</sup> IGR J015712-7259 (McBride et al. 2010), <sup>(D)</sup> SXP 265 (this work), <sup>(E)</sup> SXP 1062 (Hénault-Brunet et al. 2012), <sup>(F)</sup> RX J0123.4-7321 (Sturm et al. 2013b), <sup>(G)</sup> IGR J01217-7257 (Coe et al. 2014), <sup>(H)</sup> SXP 22.1 (Clark et al. 1997), <sup>(I)</sup> SMC X-1, <sup>(J)</sup> SXP 31.0 (Chakrabarty et al. 1998), <sup>(K)</sup> XMMU J010633.1-731543 (Coe et al. 2012).

at higher energies,  $\gtrsim 10 \text{ keV}$  (Townsend et al. 2011), and so we do not favour this model.

For all the models, the absorption of the X-ray spectrum is in agreement with or above the total line-of-sight SMC column density of  $N_{\text{H,SMC}} = 6 \times 10^{20} \text{ cm}^{-2}$  (Stanimirovic et al. 1999). This suggests the system is behind the absorbing interstellar medium in the SMC or there is some intrinsic absorbing material in close proximity to the NS. Comparing the spectrum and the spectral energy distribution of the optical counterpart suggests a rather low extinction, placing the absorbing material close to the NS.

## 4.2 Periodicities

The X-ray pulsations establish the compact object as an NS. The spin period of  $P_s = (264.516 \pm 0.014) \text{ s}$  puts the system in the population of slowly rotating pulsars (Knigge et al. 2011), which typically show wide and circular orbits with only moderate X-ray outbursts (Cheng et al. 2014). SXP 265 was consistently detected above  $F_X \sim 10^{-12} \text{ erg cm}^{-2} \text{ s}^{-1}$  when observed with sufficient sensitivity, suggesting the source exhibits a rather persistent X-ray emission at this lower level. We also observe what appears to be moderate type-I outbursts, where the X-ray luminosity increases by a factor of  $\sim 10$ – $20$ ; these are only expected during periastron. The temporal separation of these outbursts suggests an orbital period of  $P_o \sim (146 \pm 2) \text{ d}$ , however this needs further confirmation. We note that this orbital period is in agreement with the spin period, according to the Corbet relation (Corbet 1984; Laycock et al. 2005; Corbet et al. 2009).

A 6.53 d period is found in the OGLE light curve with a small amplitude of  $(0.00754 \pm 0.00028) \text{ mag}$ . There is also an indication of a feature at four times this period. Given the long spin period of the NS, the orbital period is expected to be longer ( $\gtrsim 50 \text{ d}$ ) from the Corbet relation and so we do not attribute this period to the orbit of the NS. Some BeXRBs show short-term low-amplitude variability, which is believed to be caused by non-radial pulsations (NRPs) of the Be star. These periods are usually  $< 2 \text{ d}$  (Schmidtke, Cowley &

Udalski 2013). This seems an unlikely explanation for the 6.53 d period, but these NRPs may be responsible for the 0.867 d period (in which case the 6.53 d period would be artificial). If the 0.867 d period is slightly variable with time, its power in the periodogram might decrease with respect to aliases at longer periods (Schmidtke et al. 2013). Due to the lower statistics in the latter two OGLE seasons, we cannot test the variability of the period.

## 4.3 Population comparison

The location of SXP 265 is compared with the H I column density and the distribution of the other HMXBs in Fig. 12. SXP 265 is located in the transition region between the SMC Wing and the Magellanic Bridge. The bulk of known HMXBs are found in the SMC Bar, which is known to have had an enhancement in its recent star formation. A population of sources following the tidal feature towards the LMC, i.e. the Wing and high-density western part of the Bridge, is also evident. The HMXB population appears to be less dense in the Wing (McGowan et al. 2008; Sturm et al. 2013c), but the low X-ray coverage in the outer regions of the SMC Wing and the Bridge makes it difficult to currently estimate the population of HMXB. Only three confirmed BeXRBs are currently known to be located in the Magellanic Bridge, the first was found with ROSAT by Kahabka & Hilker (2005) and two further systems were reported by McBride et al. (2010).

It is worth noting that no BeXRBs have been found elsewhere around the SMC, despite the similar coverage of the INTEGRAL and *XMM-Newton* slew surveys. This suggests that the BeXRBs in the Magellanic Bridge do not originate in the SMC Bar, as noted by McBride et al. (2010). The Bridge formed  $\sim 200 \text{ Myr}$  ago, i.e. much longer than the life time of an HMXB, and so these BeXRBs cannot have been tidally stripped from the SMC Bar population. The tidally triggered episode of star formation in the Bridge ended  $\sim 40 \text{ Myr}$  ago (Harris 2007). This is the expected evolution time of BeXRBs (Antoniou et al. 2010), and it is therefore likely that the observed BeXRBs in the Bridge were formed in this event.

Future eROSITA survey observations (Merloni et al. 2012) will reveal the population in the outer regions of the SMC with a sensitivity down to  $L_X \gtrsim 10^{35} \text{ erg s}^{-1}$ . This will allow us to further study the population of BeXRBs in a tidal structure, and might put further constraints on supernova kick velocities when the surrounding regions of the SMC have a deeper homogeneous X-ray coverage.

## 5 SUMMARY AND CONCLUSIONS

We discovered a variable X-ray source, named SXP 265, in archival *XMM-Newton* and *Swift* observations. We classified this source as a BeXRB candidate based on its correlation with a blue star in the SMC and investigated it in detail with additional follow-up observations with *XMM-Newton*, *Swift*, GROND at the MPG 2.2 m telescope, and spectroscopy at the 1.9 m Radcliffe telescope at the SAO in addition to the analysis of OGLE light-curve data.

The X-ray spectrum is typical for a HMXB with an NS compact object. The spin period of the NS is  $P_s = (264.516 \pm 0.014) \text{ s}$ . The source appears to show persistent X-ray luminosity at a few  $10^{35} \text{ erg s}^{-1}$  as well as type-I outbursts, of luminosity of a few  $10^{36} \text{ erg s}^{-1}$ , indicating a possible orbital period of 146 d.

We identify the optical counterpart at  $\text{RA} = 01^{\text{h}}32^{\text{m}}51^{\text{s}}.47$  and  $\text{Dec} = -74^{\circ}25'45''.2$  (J2000, 2MASS6X coordinates) and classify it as a B1-2II-IVe star, which has long-term variability and an excess in the NIR. An optical period is found at 0.867 d (or one of its 1-day alias) and might be explained by non-radial pulsations of the Be star. SXP 265 is located in the transition region of the SMC Wing and the Magellanic Bridge where only a few systems are known and is the second most eastern pulsar associated with the SMC.

## ACKNOWLEDGMENTS

The XMM-Newton project is supported by the Bundesministerium für Wirtschaft und Technologie/Deutsches Zentrum für Luft- und Raumfahrt (BMWi/DLR, FKZ 50 OX 0001) and the Max-Planck Society. We acknowledge the use of archival *Swift* data and thank the *Swift* team for scheduling new observations. The OGLE project has received funding from the European Research Council under the European Community's Seventh Framework Programme (FP7/2007-2013) / ERC grant agreement no. 246678 to AU. We are grateful to S. Schmidl (Thüringer Landessternwarte Tautenburg) for overlooking the GROND observation. Part of the funding for GROND (both hardware as well as personnel) was generously granted from the Leibniz-Prize to Prof. G. Hasinger (DFG grant HA 1850/28-1). PM and GV acknowledge support from the BMWi/DLR grant FKZ 50 OR 1201 and FKZ 50 OR 1208, respectively.

## REFERENCES

- Antoniou V., Zezas A., Hatzidimitriou D., Kalogera V., 2010, *ApJ*, 716, L140
- Arnaud K. A., 1996, in G.H. Jacoby, J. Barnes, eds, *Astronomical Data Analysis Software and Systems V*. Astronomical Society of the Pacific Conference Series, Vol. 101, p. 17
- Bartlett E. S., Coe M. J., Ho W. C. G., 2013, *MNRAS*, 436, 2054
- Baumgartner W. H., Tueller J., Markwardt C. B., Skinner G. K., Barthelmy S., Mushotzky R. F., Evans P. A., Gehrels N., 2013, *ApJS*, 207, 19
- Chakrabarty D., Takeshima T., Ozaki M., Paul B., Yokogawa J., 1998, *IAU Circ.*, 7062, 1
- Cheng Z. Q., Shao Y., Li X. D., 2014, *ApJ*, 786, 128
- Clark G. W., Remillard R. A., Woo J. W., 1997, *ApJ*, 474, L111
- Coe M. J. et al., 2012, *MNRAS*, 424, 282
- Coe M. J., Bird A. J., McBride V. A., Bartlett E. S., Townsend L. J., Haberl F., Kennea J., Udalski A., 2014, *The Astronomer's Telegram*, 5806, 1
- Corbet R. H. D., 1984, *A&A*, 141, 91
- Corbet R. H. D., Coe M. J., McGowan K. E., Schurch M. P. E., Townsend L. J., Galache J. L., Marshall F. E., 2009, in J.T. Van Loon, J.M. Oliveira, eds, *IAU Symposium*. IAU Symposium, Vol. 256, pp. 361–366
- D'Elia V. et al., 2013, *A&A*, 551, A142
- Dickey J. M., Lockman F. J., 1990, *ARA&A*, 28, 215
- Dufton P. L., Ryans R. S. I., Thompson H. M. A., Street R. A., 2008, *MNRAS*, 385, 2261
- Efron B., 1982, *The Jackknife, the Bootstrap and other resampling plans*
- Eger P., Haberl F., 2008, *A&A*, 491, 841
- Evans C. J., Howarth I. D., Irwin M. J., Burnley A. W., Harries T. J., 2004, *MNRAS*, 353, 601
- Evans C. J., Lennon D. J., Smartt S. J., Trundle C., 2007, *A&A*, 464, 289
- Galache J. L., Corbet R. H. D., Coe M. J., Laycock S., Schurch M. P. E., Markwardt C., Marshall F. E., Lochner J., 2008, *ApJS*, 177, 189
- Gordon K. D. et al., 2011, *AJ*, 142, 102
- Graczyk D. et al., 2014, *ApJ*, 780, 59
- Greiner J. et al., 2008, *PASP*, 120, 405
- Güver T., Özel F., 2009, *MNRAS*, 400, 2050
- Haberl F., Pietsch W., 2004, *A&A*, 414, 667
- Haberl F., Pietsch W., 2008, *A&A*, 484, 451
- Haberl F., Eger P., Pietsch W., 2008, *A&A*, 489, 327
- Haberl F., Sturm R., Filipović M. D., Pietsch W., Crawford E. J., 2012, *A&A*, 537, L1
- Harris J., 2007, *ApJ*, 658, 345
- Harris J., Zaritsky D., 2004, *AJ*, 127, 1531
- Hénault-Brunet V. et al., 2012, *MNRAS*, 420, L13
- Hickox R. C., Narayan R., Kallman T. R., 2004, *ApJ*, 614, 881
- Jansen F. et al., 2001, *A&A*, 365, L1
- Kahabka P., Hilker M., 2005, *A&A*, 435, 9
- Kahabka P., Haberl F., Payne J. L., Filipović M. D., 2006, *A&A*, 458, 285
- Knigge C., Coe M. J., Podsiadlowski P., 2011, *Nature*, 479, 372
- Krühler T. et al., 2008, *ApJ*, 685, 376
- Krühler T. et al., 2011, *A&A*, 526, A153
- La Palombara N., Mereghetti S., Sidoli L., Tiengo A., Esposito P., 2013, *Mem. Soc. Astron. Italiana*, 84, 626
- Lanz T., Hubeny I., 2007, *ApJS*, 169, 83
- Laycock S., Corbet R. H. D., Coe M. J., Marshall F. E., Markwardt C., Lochner J., 2005, *ApJS*, 161, 96
- Lennon D. J., 1997, *A&A*, 317, 871
- Li K. L. et al., 2012, *ApJ*, 761, 99
- Maggi P., Haberl F., Sturm R., Pietsch W., Rau A., Greiner J., Udalski A., Sasaki M., 2013, *A&A*, 554, A1
- McBride V. A., Coe M. J., Negueruela I., Schurch M. P. E., McGowan K. E., 2008, *MNRAS*, 388, 1198
- McBride V. A., Bird A. J., Coe M. J., Townsend L. J., Corbet R. H. D., Haberl F., 2010, *MNRAS*, 403, 709
- McClure-Griffiths N. M. et al., 2009, *ApJS*, 181, 398
- McGowan K. E. et al., 2008, *MNRAS*, 383, 330

- Merloni A. et al., 2012, ArXiv e-prints
- Morgan W. W., Keenan P. C., Kellman E., 1943, An atlas of stellar spectra, with an outline of spectral classification
- Morii M. et al., 2013, ApJ, 779, 118
- Predehl P., Schmitt J. H. M. M., 1995, A&A, 293, 889
- Rajoelimanana A. F., Charles P. A., Udalski A., 2011, MNRAS, 413, 1600
- Reig P., 2011, Ap&SS, 332, 1
- Richter O. G., Tammann G. A., Huchtmeier W. K., 1987, A&A, 171, 33
- Russell S. C., Dopita M. A., 1992, ApJ, 384, 508
- Saxton R. D., Read A. M., Esquej P., Freyberg M. J., Altieri B., Bermejo D., 2008, A&A, 480, 611
- Scargle J. D., 1982, ApJ, 263, 835
- Schlafly E. F., Finkbeiner D. P., 2011, ApJ, 737, 103
- Schmidtke P. C., Cowley A. P., Udalski A., 2013, MNRAS, 431, 252
- Shtykovskiy P., Gilfanov M., 2005, MNRAS, 362, 879
- Skowron D. M. et al., 2014, ArXiv e-prints
- Skrutskie M. F. et al., 2006, AJ, 131, 1163
- Stanimirovic S., Staveley-Smith L., Dickey J. M., Sault R. J., Snowden S. L., 1999, MNRAS, 302, 417
- Strüder L. et al., 2001, A&A, 365, L18
- Sturm R., Haberl F., Oskinova L. M., Schurch M. P. E., Hénault-Brunet V., Gallagher J. S., Udalski A., 2013a, A&A, 556, A139
- Sturm R., Haberl F., Pietsch W., Udalski A., 2013b, A&A, 551, A96
- Sturm R. et al., 2011, A&A, 527, A131
- Sturm R., Haberl F., Pietsch W., Coe M. J., Mereghetti S., La Palombara N., Owen R. A., Udalski A., 2012, A&A, 537, A76
- Sturm R. et al., 2013c, A&A, 558, A3
- Townsend L. J. et al., 2011, MNRAS, 410, 1813
- Turner M. J. L. et al., 2001, A&A, 365, L27
- Udalski A., 2008, Acta Astron., 58, 187
- Udalski A., Szymanski M. K., Soszynski I., Poleski R., 2008, Acta Astron., 58, 69
- Vasilopoulos G., Haberl F., Sturm R., Maggi P., Udalski A., 2014, A&A, 567, A129
- Walborn N. R., Fitzpatrick E. L., 1990, PASP, 102, 379
- Watson M. G. et al., 2009, A&A, 493, 339
- Wegner W., 2006, MNRAS, 371, 185
- Wilms J., Allen A., McCray R., 2000, ApJ, 542, 914